Eur. Phys. J. Spec. Top.
https://doi.org/10.1140/epjs/s11734-021-00280-0

THE EUROPEAN PHYSICAL JOURNAL SPECIAL TOPICS

Regular Article

Charging and ion ejection dynamics of large helium nanodroplets exposed to intense femtosecond soft X-ray pulses

Catherine A. Saladrigas[1,2], Alexandra J. Feinberg[3], Michael P. Ziemkiewicz[1,2,14], Camila Bacellar [1,2,15], Maximilian Bucher[4,5,6], Charles Bernando[7,16], Sebastian Carron[8], Adam S. Chatterley[1,2,17], Franz-Josef Decker[5], Ken R. Ferguson[5], Luis Gomez[3], Taisia Gorkhover[5,6], Nathan A. Helvy[1,9], Curtis F. Jones[3,18], Justin J. Kwok[10,19], Alberto Lutman[5], Daniela Rupp[6,11], Rico Mayro P. Tanyag[3,17], Thomas Möller[6], Daniel M. Neumark[1,2], Christoph Bostedt[4,5,12,13], Andrey F. Vilesov[3,7,a], and Oliver Gessner[1,b]

[1] Chemical Sciences Division, Lawrence Berkeley National Laboratory, Berkeley, CA 94720, USA
[2] Department of Chemistry, University of California, Berkeley, CA 94720, USA
[3] Department of Chemistry, University of Southern California, Los Angeles, CA 90089, USA
[4] Chemical Sciences and Engineering Division, Argonne National Laboratory, 9700 South Cass Avenue B109, Lemont, IL 60439, USA
[5] SLAC National Accelerator Laboratory, 2575 Sand Hill Road, Menlo Park, CA 94025, USA
[6] Institute of Optics and Atomic Physics, Technical University of Berlin, Hardenbergstraße 36, 10623 Berlin, Germany
[7] Department of Physics and Astronomy, University of Southern California, Los Angeles, CA 90089, USA
[8] Department of Physics, California Lutheran University, Thousand Oaks, CA 91360, USA
[9] Department of Physics, University of California, Berkeley, CA 94720, USA
[10] Mork Family Department of Chemical Engineering and Materials Science, USC, Los Angeles, CA 90089, USA
[11] LFKP, ETH Zurich, John-von-Neumann-Weg 9, 8093 Zurich, Switzerland
[12] Paul Scherrer Institut (PSI), Forschungsstrasse 111, 5232 Villigen, Switzerland
[13] LUXS Laboratory for Ultrafast X-ray Sciences, Institute of Chemical Sciences and Engineering, École Polytechnique Fédérale de Lausanne (EPFL), 1015 Lausanne, Switzerland
[14] Present address: Ball Aerospace, Boulder, CO, USA
[15] Present address: Paul Scherrer Institute, Forschungsstrasse 111, 5232 Villigen-PSI, Switzerland
[16] Present address: School of Information Systems, Binus University, Jl.K.HSyahdan No9, Palmerah, Jakarta Barat 11480, Indonesia
[17] Present address: Department of Chemistry, Aarhus University, Langelandsgade 140, 8000 Aarhus C, Denmark
[18] Present address: State University of New York (SUNY) Adirondack, Queensbury, NY 12804, USA
[19] Present address: Department of Materials Science and Engineering, University of Illinois at Urbana-Champaign, 1304 W. Green St., Urbana, IL 61801, USA

Received 14 May 2021 / Accepted 6 September 2021

Abstract Ion ejection from charged helium nanodroplets exposed to intense femtosecond soft X-ray pulses is studied by single-pulse ion time-of-flight (TOF) spectroscopy in coincidence with small-angle X-ray scattering. Scattering images encode the droplet size and absolute photon flux incident on each droplet, while ion TOF spectra are used to determine the maximum ion kinetic energy, E_{kin}, of He_j^+ fragments (j = 1–4). Measurements span He_N droplet sizes between $N \sim 10^7$ and $\sim 10^{10}$ (radii $R_0 = 78$–578 nm), and droplet charges between $\sim 9\times10^{-5}$ and $\sim 3\times10^{-3}$ e/atom. Conditions encompass a wide range of ionization and expansion regimes, from departure of all photoelectrons from the droplet, leading to pure Coulomb explosion, to substantial electron trapping by the electrostatic potential of the charged droplet, indicating the onset of hydrodynamic expansion. The unique combination of absolute X-ray intensities, droplet sizes, and ion E_{kin} on an event-by-event basis reveals a detailed picture of the correlations between the ionization conditions and the ejection dynamics of the ionic fragments. The maximum E_{kin} of He^+ is found to be governed by Coulomb repulsion from unscreened cations across all expansion regimes. The impact of ion-atom interactions resulting from the relatively low charge densities is increasingly relevant with less electron trapping. The findings are consistent with the emergence of a charged spherical shell around a quasineutral plasma core as the degree of ionization increases. The results demonstrate a complex relationship between measured ion E_{kin} and droplet ionization conditions that can only be disentangled through the use of coincident single-pulse TOF and scattering data.

[a] e-mail: vilesov@usc.edu (corresponding author)
[b] e-mail: ogessner@lbl.gov (corresponding author)

Published online: 11 October 2021

1 Introduction

X-ray free electron lasers (FELs) generate extremely intense, coherent, ultrashort pulses that have enabled single-pulse imaging of nanoscale systems, such as viruses and quantum vortices [1–4]. Interpretation of these experiments often relies on the conjecture that the pulses are sufficiently short such that the X-rays diffract before destroying the sample due to extensive ionization [5]. However, intense light-matter interactions lead to a host of complex physical processes, which can play an important role in these experiments [1,6]. Isolated and self-bound noble gas clusters are an excellent model system to study these processes via X-ray diffraction and the resulting energetics of the ionization products [7]. Here, we study the charging and ion ejection dynamics in large helium nanodroplets irradiated by intense soft X-ray pulses, exploring the relationship between the degree of ionization, charge density, and maximum ion kinetic energies.

When an atomic cluster is exposed to an intense X-ray pulse, electrons are initially "outer ionized", i.e., electrons escape the cluster following photoionization [8,9,11]. The evolution of the charging process during the continued X-ray–cluster interaction depends strongly on X-ray intensity and cluster size. In one extreme, all photoionization results in outer ionization and thus, all freed electrons escape the cluster. The charged cluster then expands via Coulomb explosion as a result of the repulsion between unscreened ions [8,9]. In the other extreme, with sufficient X-ray intensity and cluster size, the collective Coulomb potential of the cations becomes deep enough, such that the kinetic energy of photoelectrons is insufficient to escape, i.e., outer ionization is frustrated. The subsequent photoionization events result in "inner ionization", i.e., the creation of quasi-free electrons that are trapped by the Coulomb potential of the charged cluster. An early description of this processs was provided by Saalmann and Rost [10]. Assuming a homogeneous charge distribution, the Coulomb potential is deepest near the cluster center and becomes shallower toward the surface. Thus, electron trapping is expected to originate in the center of the cluster and to move outwards as ionization progresses. The result is a quasineutral plasma core that grows to encompass more of the cluster as inner ionization proceeds [12]. The hot, trapped electrons begin to thermalize with the ionic cores, and the quasineutral nanoplasma expands hydrodynamically.

In reality, the expansion dynamics of charged clusters may proceed by a combination of hydrodynamic expansion and Coulomb explosion, depending on the cluster size [13], atomic species [14], and the intensity [15] and wavelength [16] of the incident radiation [10,17]. While an extensive body of literature exists describing strong near-infrared (NIR) light–cluster interactions [12,14,16,18–20], X-ray–cluster interactions have only more recently been investigated, motivated by the availability of short, intense X-ray pulses provided by FELs. The evolution of large xenon clusters (30–600 nm) exposed to FEL pulses ($h\nu$ = 91–850 eV) with typical intensities of $\sim 10^{14}$–10^{16} W/cm^2 has been described in terms of hydrodynamic expansion and indicate that three-body recombination plays an important role in the nanoplasma dynamics [4,21]. Other studies on smaller xenon and argon clusters, as well as Xe–Ar mixed clusters, reveal a more complex situation in which the outer shell of a cluster may undergo Coulomb explosion, while the core forms a quasineutral nanoplasma, followed by hydrodynamic expansion [22–24]. Theoretical calculations predict that Ar_{923} clusters exposed to VUV (20 eV), XUV (38 eV), and soft X-ray (90 eV) pulses with the same total energy deposition exhibit a smooth transition in expansion behavior [9]. It ranges from a Coulomb explosion for soft X-rays, to hydrodynamic expansion after VUV irradiation, while the XUV-induced dynamics fall in between the two limiting cases.

Early experiments on charged clusters provided quantities, such as ion mass and/or electron energy spectra, accumulated over many pulses, and averaged over the laser fluxes and cluster sizes [12,14,18,20]. Using ultrashort, intense light sources, measurements, such as ion TOF spectra, can be acquired on a shot-by-shot basis. Although, if only ion TOF spectra are acquired, the analysis still relies on average photon fluxes and cluster sizes. More detailed information can be obtained via coincidence measurements at X-FELs, in which both the TOF spectrum and the X-ray scattering pattern are collected for each registered event. These simultaneous measurements have previously been demonstrated on highly ionized Xe clusters in the hydrodynamic expansion regime [4,21]. Here, we apply the same concept to study the transition between Coulomb explosion and hydrodynamic expansion regimes in more moderately ionized He nanodroplets. Helium atoms have only two 1s electrons. The X-ray photon energies used in this work are well above both the single and double ionization potential (IP) of helium (24.6 eV and 79 eV, respectively [25,26]) and, thus, also far from any resonances. The resulting X-ray scattering patterns can be analyzed in a straightforward fashion using the Rayleigh–Gans approximation [3,27] to determine the droplet size and the absolute single-pulse photon flux incident on the droplet. The validity of this approximation and the simplicity of the helium atom electronic structure enable an accurate determination of the incident photon flux and a relatively simple theoretical description of the charging process by photoionization, devoid of both high charge states and Auger cascades.

In this work, we monitor the interaction of single intense X-ray pulses ($h\nu$ = 838 eV, $\sim 10^{11}$ photons/pulse) with individual large helium droplets (radius R_0 = 78–578 nm) via coincident single-pulse coherent X-ray scattering and ion TOF spectroscopy. The unique event-by-event measurements provide detailed access to droplet charging and ion ejection dynamics across a large range of ionization regimes, from nominally pure Coulomb explosion conditions well

into the quasineutral nanoplasma regime. Simultaneous measurements of the absorbed number of photons, the droplet size, and the ion TOF spectrum for each event provides unprecedented detail on the degree of ionization and corresponding ion kinetic energy release of each individual cluster. Measurements span He_N droplet sizes between $N \sim 10^7$ and $\sim 10^{10}$, and droplet charges between $\sim 9\times10^{-5}$ and $\sim 3\times10^{-3}$. In terms of the dimensionless frustration parameter α (see below) [9], ionization conditions cover a range of $\alpha = 0.23$–44.

In all ionization regimes accessible in this experiment, the observed maximum ion kinetic energy ($E_{\mathrm{kin}}^{\mathrm{max}}$) values are consistent with a theoretical model in which the ion E_{kin} are governed by a combination of Coulomb repulsion in the collective cluster potential from unscreened ions and ion–atom interactions during the expansion. In the predominantly Coulomb explosion regime (small α), screening by trapped electrons is negligible and unscreened charges are homogeneously distributed throughout the cluster. The resulting ion TOF spectra are heavily impacted by interactions of ions with neutral atoms during the expansion process, due to the relatively low overall charge density in this study. In the predominantly hydrodynamic expansion regime (large α), frustrated ionization is initiated at the droplet center and expands outward, leading to increased localization of unscreened charges near the surface of the nanoplasma with increasing α. In this regime, the fastest ions contained in the TOF spectra predominantly reflect ions originating from the surface and their kinetic energies are well captured by a model of an expanding thin, charged spherical shell, driven by Coulomb repulsion.

2 Experiment

The experiment is conducted using the LAMP chamber at the AMO instrument of the Linac Coherent Light Source (LCLS) [28–30]. A schematic of the experiment is illustrated in Fig. 1. A beam of helium droplets is produced upon the expansion of 99.9999% purity liquid helium into vacuum through a 5 µm nozzle cooled to 5.8 K at a backing pressure of 20 bar. The measured average He_N droplet size is $\langle N\rangle \sim 2\times10^9$, which is very close to the expectation value of $\langle N\rangle \sim 1\times10^9$ from previous measurements at same conditions [31]. The droplet beam is intersected by short X-ray pulses ($\sim$ 65 fs FWHM, $h\nu = 838$ eV) that are delivered at a 120-Hz repetition rate. The X-rays are focused using a pair of KB mirrors to a nominal 2.5 μm^2 spot size in the interaction region. Based on the LCLS operating parameters and previous beamline transmission measurements, average pulse fluxes on the order of $\sim 10^{16}$ W/cm^2 ($\sim 10^{23}$ photons/m^2) are expected in the interaction region. As described in the following, the exact values for each X-ray–cluster interaction are determined from the single-pulse scattering patterns. Scattered X-ray photons are detected with a two-panel pnCCD detector, 710 mm downstream from the X-ray focus. The active regions of the detector panels are separated by a gap of 1.5 mm and each panel has an additional 4.4×1.8 mm^2 gap to let the primary X-ray beam pass through. The detector records small angle X-ray scattering patterns $\left(q \sim 2\times10^{-3} - 2\times10^{-2}\,\mathring{A}^{-1}\right)$. About the interaction region, an ion TOF spectrometer [28] is aligned perpendicular to both the helium droplet and X-ray beams, detecting cations produced upon the X-ray absorption. A 10 mm × 1 mm slit aperture is mounted on the ion extraction electrode and aligned perpendicular to the FEL beam to suppress detection of ionized background gas outside the FEL focus. The aperture also provides more direct access to the E_{kin} distribution of ejected cations, as TOF averaging effects due to ion emission angular distributions are greatly reduced. X-ray diffraction images (Fig. 1b) and ion TOF spectra (Fig. 1c) are recorded in coincidence for each detectable scattering event from a single droplet.

3 Results

3.1 Individual droplet sizes and absolute on-target photon fluxes

Over 30 minutes of data acquisition, 47 scattering images with sufficient signal for post-analysis were recorded. A typical scattering pattern is shown in Fig. 1b. Quantitative analysis of the single-pulse X-ray scattering patterns using the Rayleigh–Gans approximation for optically thin targets [3,27] provides direct access to both the size of individual droplets as well as the photon flux interacting with them. For small angle scattering in the Rayleigh–Gans regime, the ring spacing in scattering patterns such as in Fig. 1b can be approximated by $\Delta\Theta \approx \frac{\lambda}{2R_0}$, where λ is the X-ray wavelength, R_0 is the droplet radius and $\Delta\Theta$ is the difference in scattering angles between rings. Fits to an analytical expression for the diffraction intensity, as described in Gomez et al. [3], are used to derive the droplet radius. Based on the number density of liquid ^{4}He at a temperature of 0.4 K, $\nu_{LHe} = 2.18\times10^{28}$ m^{-3} [32], the number of atoms in the droplet, N, is determined from the radius by $N = \frac{4}{3}\pi R_0^3 \nu_{LHe}$ [33]. It has previously been observed that a fraction of droplets in beam expansions have spheroidal shapes due to centrifugal distortion [34,35]. However, consistent with previous measurements in comparable size regimes [35], droplets studied here have an average aspect ratio of 1.05 and, for the purpose of this work, are approximated as spheres.

The flux F (photons/m^2) of the X-ray pulse interacting with the droplet is obtained from the total number of scattered photons, which is given by

$$I_{\mathrm{total}} = \frac{8\pi^3 R_0^4 \left|n-1\right|^2}{\lambda^2} F, \tag{1}$$

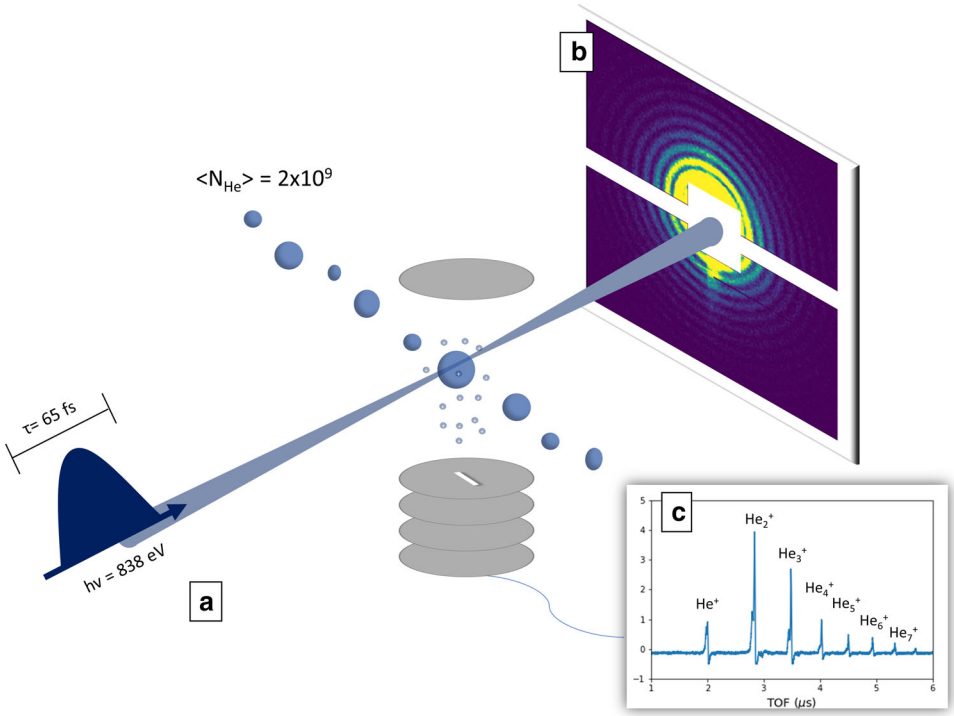

Fig. 1 **a** Diagram of experimental setup. A pulsed X-ray light source is focused down to intersect the helium droplet jet. Down stream of the interaction region, a pair of pnCCD's detect small angle X-ray scattering. About the interaction region, an ion-TOF spectrometer detects cationic products. **b** Sample diffraction image. **c** Coincident ion TOF spectrum

where n is the complex refractive index of liquid helium, n = 1–4.32 $\times 10^{-5} + 1.75 \times 10^{-7} i$ [3,36]. The value of n is obtained from the atomic scattering factors for He atoms [37] of $f_1^0 = 2.02$ and $f_2^0 = 8.16 \times 10^{-3}$ at 838 eV ($\lambda = 1.5$ nm), the number density of liquid helium of ν_{LHe} , and the classical electron radius $r_e = 2.818 \times 10^{-15}$ m according to [36]:

$$n = 1 - \frac{\nu_{\mathrm{LHe}} r_e \lambda^2 (f_1^0 - i f_2^0)}{2\pi}. \tag{2}$$

The value of I_{total} is obtained by scaling the total scattering intensity from a droplet with radius R_0 to the range of observable scattering vectors, which excludes the central hole in the detector and the gap between the CCD plates. The scattered intensity is expressed in photon units using the calibrated detector single photon response. The number of the absorbed photons is obtained as follows [36]:

$$N_{\mathrm{abs}} = 2 r_e \lambda \times f_2^0 \frac{4\pi R_0^3}{3} \nu_{\mathrm{LHe}} F. \tag{3}$$

In this work, droplet radii range from $R_0 = 78$ to 578 nm, and the photon flux ranges from $F = 1.3 \times 10^{21}$ to 5.7×10^{22} photons/m^2. The droplet radius is determined within $\sim 5\%$ and the photon flux is accurate within $\sim 20\%$ with the uncertainty arising from approximating the droplets as spheres, the detector noise subtraction, and from using a nominal detector signal-to-photon count conversion factor. This so-called analog-to-digital unit (ADU) is affected by parameters such as the detector gain and quantum efficiency and may principally vary over the detector lifetime. The variation in photon flux mostly results from the spatial distribution of the detected droplets with respect to the FEL beam axis. Some additional variation originates from the pulse-to-pulse intensity fluctuations of the FEL.

At a photon energy of 838 eV, photoabsorption leads to photoionization with the number of absorption events given by Eq. 3. We neglect single-photon double ionization events in these estimates, since the relative cross section for double vs. single ionization at 838 eV photon energy is less than 3% [26]. As such, the number of ions resulting from photoionization, N_{ion}, is equal to N_{abs}. Note that N_{ion} does not necessarily correspond to the number of electrons leaving the droplet. Additionally, N_{ion} does not include ions resulting from secondary ionization.

3.2 Helium cation TOF spectra

Cation TOF spectra provide information about the relative abundance of different cation species produced in the X-ray–cluster interaction, as well as the ion kinetic energies. An example cation cluster spectrum is shown in Fig. 1c. The leftmost (i.e., shortest TOF) feature corresponds to the singly charged He^+ atomic ions, with the features following at longer times of flight corresponding to He_j^+ clusters with $j > 1$. Numerical ion trajectory simulations (SIMION®) are used to convert from TOF to initial ion kinetic energy in the interaction region. The analysis is focused on the short-TOF edge of the peaks, corresponding to the maximum ion kinetic energy, since many peaks exhibit strong saturation effects at longer TOF. Additionally, the particular layout and operating voltages of the TOF spectrome-

ter leads to the unusual situation where almost all ions with nonzero initial kinetic energy, independent of their emission direction, arrive at the detector before the zero kinetic energy ions. Even most ions originally ejected away from the detector are accelerated such that they overtake the zero kinetic energy ions in the drift region of the spectrometer and their TOF signals overlap with ions emitted toward the detector. Thus, the recorded TOF spectra were calibrated by using the longest TOFs of the He_j^+, $j = 1, 2, \ldots, 8$ signals to identify the $E_{kin} = 0$ positions of the different mass peaks. The origin of the TOF axis (TOF = 0) is additionally defined by a peak caused by scattered X-rays and another peak from residual hydrogen ions was included in the calibration as well at very short TOF. The precision of the calibration was maximized by using the weakest intensity hits that contained the required mass peaks, which circumvents potential issues with signal modulations at the long-TOF peak edges in the more intense hits caused by electronic ringing. Due to the overlap of signals from ions ejected both toward and away from the detector, it is rather challenging to recover the complete ion kinetic energy distribution from the TOF signals. However, ions ejected toward the detector with the highest kinetic energies are always the first to arrive at the microchannel plate. Therefore, the maximum ion kinetic energies E_{kin}^{max} can be faithfully recovered from the shortest TOF.

Uncertainty in determining E_{kin}^{max} arising from electronic signal noise dominates for weaker hits (and correspondingly for ion features with smaller E_{kin}^{max}). Systematic uncertainties arising from the limited precision in locating the interaction region with respect to the center of the ion TOF spectrometer dominate for strong hits and higher E_{kin}^{max}. In particular, for He^+, which will be the focus of the discussion, the smallest E_{kin}^{max} values are determined within 20% and the largest within 6% uncertainty. E_{kin}^{max} is determined for He^+, as well as He_2^+, He_3^+ and He_4^+ when present. For example, the E_{kin}^{max} corresponding to the TOF spectrum in Fig. 1c are 103, 123, 24, and 8 eV, respectively, for the four ion species.

3.3 Size- and charge-dependent TOF spectra

Figure 2 illustrates some of the information revealed by the combination of single-pulse TOF spectra with single-pulse scattering images. The ion TOF spectra in Fig. 2 are grouped into four panels according to the droplet size (horizontal axis). Panels a, b, c, d correspond to droplets having $\sim 10^7, \sim 10^8, \sim 10^9$ and $\sim 10^{10}$ atoms, respectively. The respective color codes of black, blue, green, and red, are also used in Figs. 3, 4, 5 and 6 to identify droplet sizes associated with different data points. In each panel the TOF spectra are offset corresponding to the number of photoionization events per atom of the droplet, N_{ion}/N (vertical axis). In each spectrum, the peak with the smallest TOF ($\sim 2\,\mu s$) corresponds to He^+ ions, followed by He_j^+ fragments with $j = 2, 3, 4, \ldots$ with increasing TOF. All spectra in Fig. 2 are plotted using the same scale.

Several trends are readily apparent in Fig. 2. As the droplet size increases for a given average charge per atom (i.e., for constant photon flux), the corresponding TOF spectra extend to increasingly larger helium cation clusters. For example, for $N_{ion}/N \approx 2$–3×10^{-4} e/atom, the largest detected He_j^+ cluster size increases from $j = 3$ for $N \sim 10^7$ to $j = 8$ for $N \sim 10^{10}$. Conversely, within a given size regime, the He_j^+ size distribution shifts from larger to smaller values of j with increasing average charge. In particular, at $N_{ion}/N = 1.8 \times 10^{-3}$ e/atom no $He_{j\geq 3}^+$ ions are observed whereas the monomer peak becomes the most intense spectral feature for all droplet sizes. Additionally, a further increase in N_{ion}/N leads to a broadening of the $He_{j=1,2}^+$ peaks towards shorter times of flight, corresponding to an increase in the ion kinetic energy. Note that we do not observe any signatures of He^{++} fragments in the TOF spectra, which would be expected at TOF ~ 1.4 μs.

4 Analysis

4.1 Cluster charging and degree of frustrated ionization

As an intense X-ray pulse passes through the target, the series of ionization events leads to a concomitant increase of the collective Coulomb potential of all ions in the droplet. Assuming a homogeneous distribution of ionization events, [17] the cluster Coulomb potential experienced by an electron can be described by

$$V_{Coul}(r) = \begin{cases} -\frac{e}{4\pi\epsilon_0}\frac{N_{eff}}{2R_0}\left(3 - \frac{r^2}{R_0^2}\right), & r < R_0 \\ -\frac{e}{4\pi\epsilon_0}\frac{N_{eff}}{r}, & r \geq R_0 \end{cases} \quad (4)$$

Here, e is the elementary charge, ϵ_0 is the permittivity of free space, and r corresponds to the distance from the droplet's center. N_{eff} is the net number of charges contributing to the Coulomb potential as described in the following. According to Eq. 4, the kinetic energy of the primary photoelectrons, $E_{kin}(e^-) = h\nu - IP \lesssim 813.4$ eV (IP: atomic ionization potential), will be insufficient to overcome the cluster Coulomb potential if the droplet's charge reaches a critical value. At this point, the locally freed electrons will be trapped as quasi-free electrons and begin to form a nanoplasma. The potential in Eq. 4 is deepest at $r = 0$. Thus, frustration of ionization is expected to commence at the droplet center and expand outward with increasing degree of ionization during the passage of a sufficiently intense X-ray pulse through the target. With the onset of photoelectron trapping, the effective number of ions contributing to the Coulomb potential, i.e., the net droplet charge, is smaller than the total number of created ions, $N_{eff} < N_{ion}$, due to partial screening of the ionic back-

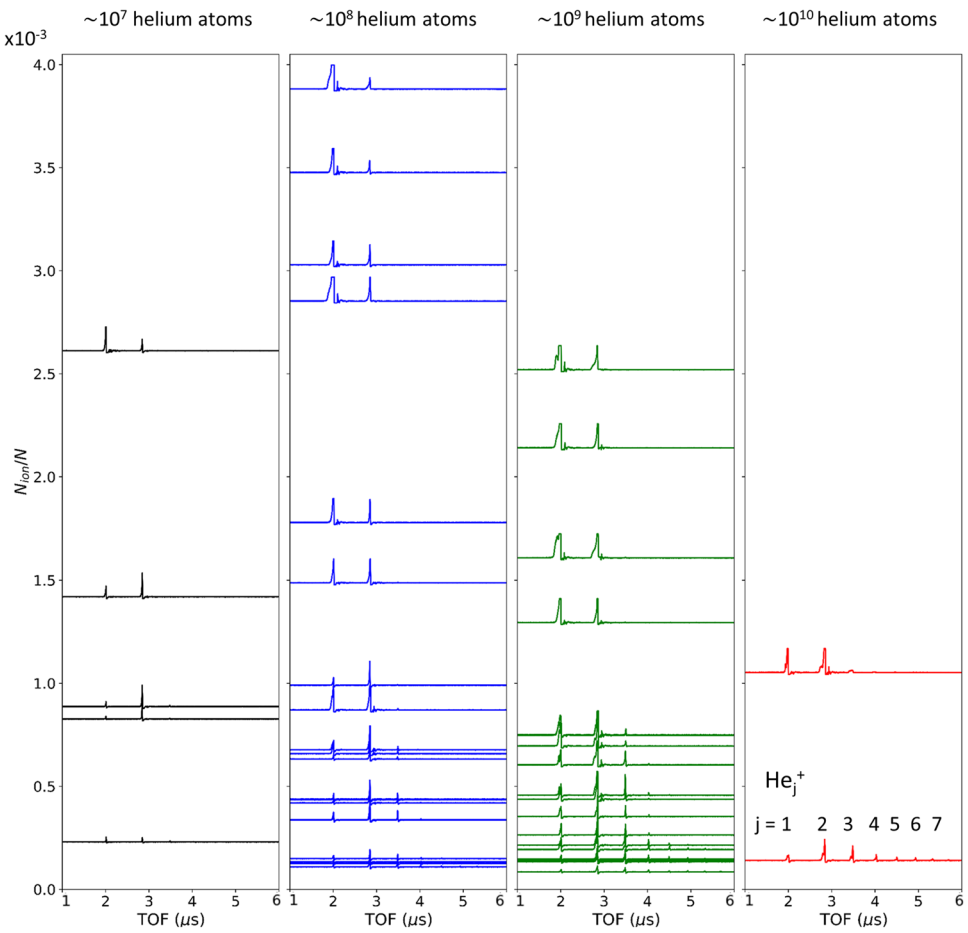

Fig. 2 Helium droplet ion TOF spectra are vertically sorted by the number of photoabsorption events, normalized to the number of helium atoms (which is approximately synonymous to the average droplet charge, neglecting secondary ionization events). Panels **a**–**d** feature TOF spectra obtained in droplets of different sizes ($\sim 10^7, 10^8, 10^9$ and 10^{10} atoms). The size regimes are further indicated by the colors of the TOF spectra, and the same color code is used in all subsequent figures

ground by trapped electrons. Note that the term for $r < R_0$ in Eq. 4 is nominally only valid for conditions before the onset of frustration, as trapped electrons will move towards the center of the charged cluster and, therefore, the net charge distribution is no longer homogeneous [17]. In addition, this discussion neglects any secondary ionization events.

The degree of ionization frustration is quantified by the dimensionless frustration parameter [9]

$$\alpha = \frac{N_{\mathrm{ion}}}{N_{\mathrm{frust}}} \tag{5}$$

whereby N_{frust} is the effective number of droplet charges needed to completely frustrate outer ionization across the entire droplet. N_{frust} can be determined by equating the maximum kinetic energy $E_{\mathrm{kin}}(e^-) = 813.4$ eV of an electron to its Coulomb energy at the surface of a cluster with radius R_0, according to Eq. 4 leading to

$$N_{\mathrm{frust}} = \frac{4\pi\epsilon_0}{e^2} E_{\mathrm{kin}}(e^-) R_0 \approx 565 \cdot R_0\,(\mathrm{nm}). \tag{6}$$

From Eqs. 4–6 it follows that frustrated ionization sets in at the droplet center for $\alpha = 2/3$ and full frustration is reached at $\alpha \gtrsim 1$, after which all additional photon absorption leads to inner ionization. Note that α needs to be somewhat larger than 1 to reach full frustration as electron trapping from the core outwards leads to partial screening of ions and thus, not all N_{ion} ions created by photoionization contribute to the droplet charge, with the exact value depending on the conditions of the given system. The degree of frustration has direct impact on the droplet expansion dynamics following ionization, with Coulomb explosion dominating for $\alpha \lesssim 1$ and hydrodynamic expansion of the nanoplasma for $\alpha \gg 1$. At intermediate values with α on the order of ~ 10, the expansion does not clearly fall into either of these limiting categories [9]. We emphasize that the frustration parameter is a measure of frustration based on photoionization alone. Taking into account electron impact ionization, the number of ionization events may principally be larger by up to a factor of ~ 30, based on the ratio between the photon energy and the He atom IP. However, with increasing charge density and the emergence of lower E_{kin} electrons, there is also an increased likelihood of electron-ion recombination. As such, the total number of ions evolves with time in a complex fashion that is beyond the scope of this work. We therefore resort to define the frustration parameter based on the initial

ionization conditions alone, which are directly accessible within our experiment.

From $N_{\mathrm{ion}} \propto FR_0^3$ it follows that $\alpha \propto FR_0^2$, elucidating the relationship between X-ray intensity, droplet size, and expansion regime. Note, in particular, that both the X-ray intensity and the droplet size contribute independently to the degree of ionization frustration. Thus, both need to be determined on an event-by-event basis in order to evaluate the regime of ionization for every X-ray–droplet interaction. The results presented herein are associated with frustration parameters between $\alpha = 0.23$ and $\alpha = 44$, spanning the entire range from pure Coulomb explosion to significant ionization frustration, expected to lead predominantly to hydrodynamic expansion.

4.2 Relation between maximum kinetic energy release and degree of frustration

Different cluster disintegration mechanisms typically give rise to different kinetic energies of the ions [18, 38,39]. Thus, it is instructive to plot the maximum detected ion kinetic energy $E_{\mathrm{kin}}^{\mathrm{max}}$ against the frustration parameter α. This relation is shown for He^+, He_2^+, He_3^+ and He_4^+ ions in Fig. 3a–d, respectively. For monomer and dimer cations, a clear trend emerges, whereby $E_{\mathrm{kin}}^{\mathrm{max}}$ increases continuously with increasing α for $\alpha \lesssim 20$ and appears to saturate for larger degrees of frustration. For trimers and tetramers, no clear trend emerges. However, the characteristic kinetic energies decrease with increasing size j of the He_j^+ fragments. Representative error bars are included in all panels, which are estimated based on systematic uncertainty for the high $E_{\mathrm{kin}}^{\mathrm{max}}$ and electronic signal noise for small $E_{\mathrm{kin}}^{\mathrm{max}}$, as described in Sect. 3.2.

Note that the monomer and dimer cation trends, while qualitatively similar, differ on a quantitative level. The maximum kinetic energies of the monomer cations in the plateau region exceed those of the dimer cations by approximately a factor of two. We speculate that this effect may be the result of a combination of two underlying phenomena. With increasing flux and therefore a higher degree of frustration, we observe a decrease in cationic cluster yield compared to monomer fragment yield (see Fig. 2). One can infer that fragments larger than monomers are less likely to survive the most energetic expansion conditions that produce the fastest He^+ ions. Consequently, the fastest He_j^+ ions may be formed and ejected during different phases of the expansion compared to the He^+ fragments. Other works [22–24] suggest contributions from different expansion stages to detected ion mass and kinetic energy distributions, whereby the outer shell of unscreened ions undergo a Coulomb explosion while the remaining plasma core undergoes a hydrodynamic expansion. If the $He_{j\geq 2}^+$ products form in the later stages of the shell explosion and/or in the plasma core, this could lead to lower ion kinetic energies.

In the following discussion, we will use the results for He^+ ions in Fig. 3a to derive a quantitative model for explaining the observed kinetic energy dependences based on Coulomb repulsion and ion-atom scattering effects. Results for He_j^+ clusters are not included in the discussion. Such clusters are formed upon attachment of one or more He atoms to He^+ ions, with complex dynamics that are beyond the scope of this work.

5 Discussion

Figure 3a indicates a close relationship between the degree of frustration reached during the X-ray–cluster interaction and the maximum kinetic energy of ejected He^+ ions. The physical origin of the observed trend, however, is not readily apparent and requires additional analysis and modeling. Both Coulomb explosion and hydrodynamic expansion may contribute to ion kinetic energy distributions across the range of α values studied here. $E_{\mathrm{kin}}^{\mathrm{max}}$, however, is expected to be defined by Coulomb repulsion effects, as indicated by the following estimates. The average ion kinetic energy $\left\langle E_{\mathrm{kin}}^{\mathrm{Hyd}} \right\rangle$ in a hydrodynamic expansion is described by [40]

$$\left\langle E_{\mathrm{kin}}^{\mathrm{Hyd}} \right\rangle = \frac{3}{2} k_b T_e \frac{N_{\mathrm{ion}}}{N}, \tag{7}$$

where N_{ion}/N is the average charge per atom, k_b is the Boltzmann constant, and T_{e} is the initial electron temperature of the nanoplasma. N_{ion}/N is derived from the scattering images as described above, and the remainder of the right-hand term in Eq. 7 is estimated by the kinetic energy of the photoelectrons $\frac{3}{2}k_b T_{\mathrm{e}} \simeq 813.4$ eV. With N_{ion}/N varying between $\sim 9 \times 10^{-5}$ and $\sim 3 \times 10^{-3}$, $\left\langle E_{\mathrm{kin}}^{\mathrm{Hyd}} \right\rangle$ ranges from ~ 0.07 to 2 eV. These values are ~ 2 orders of magnitude smaller than the observed maximum kinetic energies $E_{\mathrm{kin}}^{\mathrm{max}}$ (Fig. 3). We estimate that the inclusion of electron impact ionization would bring $\left\langle E_{\mathrm{kin}}^{\mathrm{Hyd}} \right\rangle$ at most to within one order of magnitude of $E_{\mathrm{kin}}^{\mathrm{max}}$. Thus, we proceed by comparing $E_{\mathrm{kin}}^{\mathrm{max}}$ to the Coulomb potential energy experienced by an ion at the surface of the charged droplet.

5.1 Surface Coulomb potential energy

The potential energy of an ion at the droplet's surface ($r = R_0$) is $U_{\mathrm{Coul}}(r = R_0) = \frac{e^2}{4\pi\epsilon_0}\frac{N_{\mathrm{eff}}}{R_0}$, taking into account the screening of ions by trapped electrons. The effective number of unscreened charges, N_{eff}, contributing to the Coulomb potential is approximated by the difference between the total number of ions and the number of trapped electrons: $N_{\mathrm{eff}} = N_{\mathrm{ion}} - N_{\mathrm{trap}}$. The underlying assumption is that, on average, each trapped electron screens one cationic charge. N_{eff} is estimated for three distinct frustration regimes: (i) $\alpha < 0.67$, (ii) $0.67 \leq \alpha \lesssim 2.5$, and (iii) $\alpha \gtrsim 2.5$. See Appendix A for a more detailed discussion of the underlying frustration regimes.

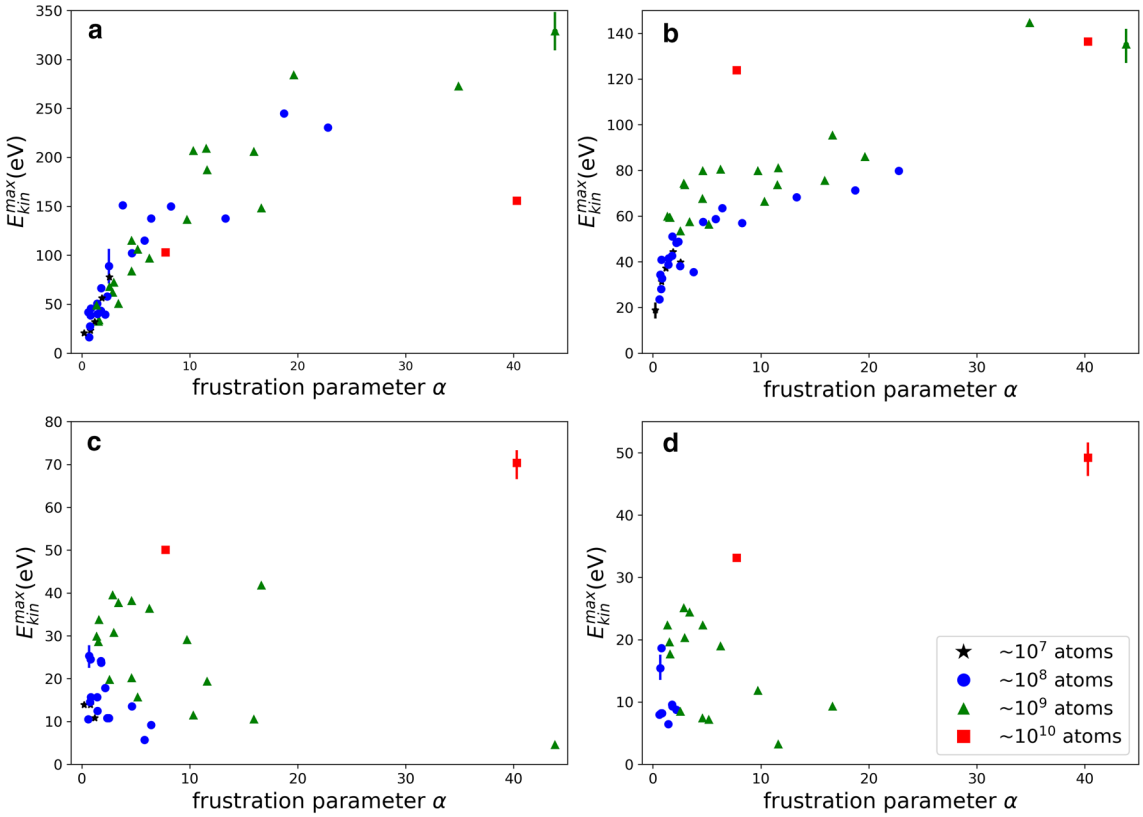

Fig. 3 Maximum ion kinetic energies, $E_{\mathrm{kin}}^{\mathrm{max}}$ derived from the shortest flight times in the ion TOF spectra and plotted as a function of the frustration parameter α for **a** monomer, **b** dimer, **c** trimer, and **d** tetramer cations

(i) For $\alpha < 0.67$, the Coulomb potential according to Eq. 4 is insufficient for electron trapping throughout the entire cluster. Thus, the number of unscreened charges is equivalent to the total number of ions, i.e, $N_{\mathrm{eff}} = N_{\mathrm{ion}}$.

(ii) The range $0.67 \leq \alpha \lesssim 2.5$ corresponds to partial frustration, in which electron trapping is achieved within a radius, $0 < r_{\mathrm{frust}} < R_0$, as governed by the cluster Coulomb potential. A finite step simulation is implemented, as described in Appendix A, to determine the number of trapped electrons, N_{trap} in this regime. N_{eff} is then estimated as $N_{\mathrm{eff}} = N_{\mathrm{ion}} - N_{\mathrm{trap}}$.

(iii) For $\alpha \gtrsim 2.5$, full frustration is achieved at time t_f, with $r_{\mathrm{frust}}(t_f) = R_0$. All additional ionization at times $t > t_f$ is subject to electron trapping and does not contribute to the effective number of charges. Thus, N_{eff} can be estimated by $N_{\mathrm{eff}} = N_{\mathrm{frust}}$.

We note that these estimates neglect electron-electron collisions, which other studies have observed contribute to outer ionization in dense nanoplasmas, thus leading to a higher net charge [41]. However, as this effect is strongly dependent on the density of trapped electrons, it is not expected to play an important role in the study herein, with electron densities ~ 3 orders of magnitude smaller than ν_{LHe}.

Figure 4 shows the ratio of the measured $E_{\mathrm{kin}}^{\mathrm{max}}$ and the surface Coulomb potential energy, U_{Coul} based on the effective number of unscreened charges N_{eff} as described above. The color codes of the data points indicate the same size regimes as in Figs. 2 and 3. A continuous trend emerges, in which $E_{\mathrm{kin}}^{\mathrm{max}}$ is always smaller than the Coulomb energy of a He^+ ion at the outermost cluster surface ($r = R_0$), and $E_{\mathrm{kin}}^{\mathrm{max}}/U_{\mathrm{Coul}}$ varies between ~ 0.03 and ~ 0.4 across different frustration regimes. The similarities in Figs. 3a and 4 arises from the fact that the surface potential is constant for $\alpha \gtrsim 2.5$.

5.2 $E_{\mathrm{kin}}^{\mathrm{max}}$ in the highly frustrated regime

As shown by Fig. 4, as α exceeds ~ 20, $E_{\mathrm{kin}}^{\mathrm{max}}/U_{\mathrm{Coul}}$ begins to plateau, approaching a ratio of ~ 0.4. In this highly frustrated regime, due to substantial electron trapping, unscreened ions occupy less than 4 nm (see Sect. 5.4 and Appendix C) of the outermost shell of the charged droplet, with the remainder of the droplet comprising of a quasineutral core. The range of radii corresponds to less than 2% of the droplet radius. As such, we model the ion ejection in this regime as the expulsion of a thin spherical shell of N_{eff} unscreened ions. Within this model, the average ion kinetic energy $E_{\mathrm{kin}}^{\mathrm{shell}}$ corresponds to the stored energy per ion of a spherical shell as follows:

$$E_{\mathrm{kin}}^{\mathrm{shell}} = E_{\mathrm{shell}}/N_{\mathrm{eff}} = \frac{1}{2}\frac{e^2}{4\pi\epsilon_0}\frac{N_{\mathrm{eff}}}{R_0} = \frac{1}{2}U_{\mathrm{Coul}}. \quad (8)$$

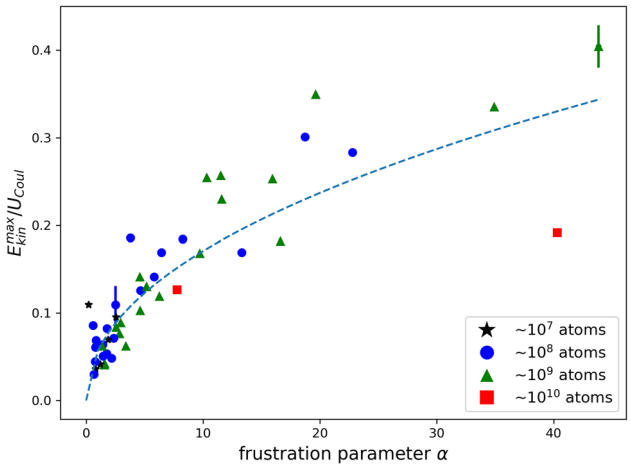

Fig. 4 Ratio of the maximum He^+ kinetic energy and the Coulomb energy of singly charged ions at the droplet surface. To better clarify the trend discussed in Sect. 5, a dashed blue trend line is plotted over the data points, corresponding to $E_{\mathrm{kin}}^{\mathrm{max}}/U_{\mathrm{Coul}} \propto \sqrt{\alpha}$. See Appendix B for more details

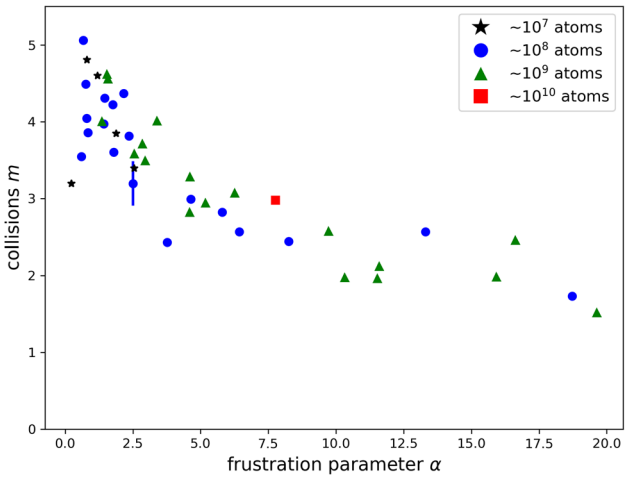

Fig. 5 Minimum number of ion–atom collisions required to decelerate the ion from the value of the Coulomb energy at the cluster surface to the measured maximum kinetic energy

The ratio of 1/2 between the average E_{kin} per ion and the Coulomb potential is very close to the observed value of ~ 0.4 in the highly frustrated regime, supporting the picture that a thin spherical shell expansion captures the dominant physics for $\alpha \gtrsim 20$.

5.3 $E_{\mathrm{kin}}^{\mathrm{max}}$ in the weakly frustrated regime

The expected maximum ion E_{kin} for a Coulomb explosion of a homogeneously charged sphere is equivalent to U_{Coul} [42]. However, for $\alpha < 20$, the measured maximum ion kinetic energies are significantly smaller, with $E_{\mathrm{kin}}^{\mathrm{max}}/U_{\mathrm{Coul}}$ reaching values as small as $\sim 1/30$ in the non-frustrated regime, where pure Coulomb explosion is expected (Fig. 4). We propose that this, at first glance, counterintuitive trend is the result of ion–atom interactions throughout the expansion process. Due to the relatively low charge densities herein, ionization of the droplets initiates a Coulomb explosion of unscreened ions within a dense medium of neutral atoms. Ion–atom interactions within the charged droplet impart energy on the neutral atoms and, thus, the expansion will likely be marked by a more collective motion of neutral atoms and ions than in the highly frustrated regime. While a detailed modeling of this motion is beyond the scope of this work, it is instructive to analyze the ratio of the observed $E_{\mathrm{kin}}^{\mathrm{max}}$ and the surface Coulomb potential U_{Coul} within a picture of a number of (hypothetical) ion-neutral collisions that would be required for ions with initial kinetic energy of U_{Coul} to decelerate to the observed $E_{\mathrm{kin}}^{\mathrm{max}}$.

The effect of each collision in this picture on the asymptotic ion kinetic energy depends on the ion's distance from the cluster surface upon colliding with another atom. At short distances, the absolute E_{kin} loss will be small, while it is at a maximum in the limit of large distances. We choose to estimate the minimum number of collisions required to account for the observed differences between the cluster surface Coulomb potential and the observed maximum ion kinetic energy. In other words, we estimate the number of collisions experienced by an ion that has already achieved its terminal velocity. We treat ion-atom collisions within a hard spheres model with equal mass and size of the collision partners, He^+ and He. The average He^+ kinetic energy loss per collision is estimated by assuming elastic collisions of an ion with a He atom at rest. With the probability of a given impact parameter scaling linearly with impact parameter [43], averaging over all collision geometries yields a mean kinetic energy loss per collision of 50%.

Upon undergoing m collisions, the ion kinetic energy, $E_{\mathrm{kin}}^{m,th}$, is:

$$E_{\mathrm{kin}}^{m,th} = U_{\mathrm{Coul}} \cdot 0.5^{\mathrm{m}}. \tag{9}$$

By equating $E_{\mathrm{kin}}^{m,th}$ with the measured values $E_{\mathrm{kin}}^{\mathrm{max}}$, the minimum number of collisions can be estimated, as is plotted in Fig. 5. We observe a decrease in the minimum number of collisions, with a continuous trend that ranges from $m \gtrsim 5$ at small α to $m \gtrsim 1.5$ as we approach $\alpha \sim 20$. This decrease in number collisions correlates with the increasing plasma core size relative to the droplet diameter, and therefore localization of unscreened ions towards the droplet surface, as the frustration parameter increases. Note that m is representative of the net likelihood for unscreened ions to interact with neutral atoms and does not refer to the individual probability of an ion–atom collision. Furthermore, we note that the underlying physics governing ionic motion is not encompassed in this heuristic model, as this is presently unknown and beyond the scope of this work.

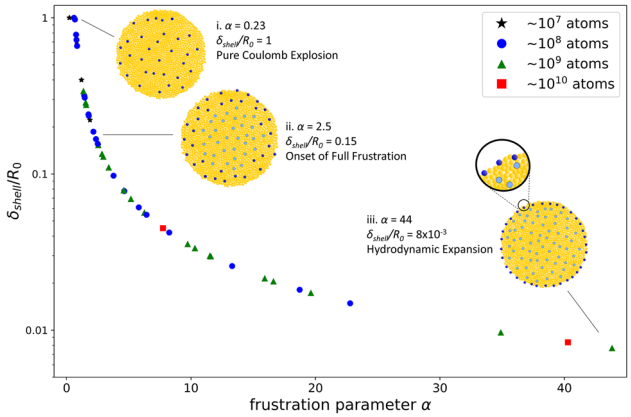

Fig. 6 Thickness of the shell of unscreened ions normalized to the droplet radius versus the frustration parameter. Pictograms indicate the structure of the charged droplets, which are modeled by charged shells of unscreened ions (dark blue) surrounding a quasineutral plasma core (light blue), interspersed amongst neutral helium atoms (yellow). The three illustrations correspond to different ionization/expansion regimes: (i) no frustration, (ii) onset of full frustration, and (iii) highest observed degree of frustration

5.4 Illustration of droplet charge distributions

In order to visualize the relationship between frustration and shell thickness within the model of a homogeneously charged spherical shell, we derive a mathematical relationship between δ_{shell}, R_0, N_{eff}, and N_{ion}. The thickness of the shell of unscreened ions, δ_{shell}, can be calculated using the number of unscreened ions, N_{eff}, from Sect. 5.1, the overall cation charge density $\rho_{\mathrm{He}^+} = N_{\mathrm{ion}}/(\frac{4}{3}\pi R_0^3)$, and by assuming a sharp boundary between the screened and unscreened ions. The shell thickness, δ_{shell}, is then related to N_{eff} and ρ_{He^+} by:

$$N_{\mathrm{eff}} = \frac{4}{3}\pi \left[R_0^3 - (R_0 - \delta_{\mathrm{shell}})^3\right] \rho_{\mathrm{He}^+}. \qquad (10)$$

From this we derive the following relationship:

$$\delta_{\mathrm{shell}}/R_0 = 1 - (1 - \frac{N_{\mathrm{eff}}}{N_{\mathrm{ion}}})^{1/3}. \qquad (11)$$

Note that $N_{\mathrm{eff}} = N_{\mathrm{frust}}$ for $\alpha \gtrsim 2.5$, and thus $N_{\mathrm{eff}}/N\mathrm{ion} = 1/\alpha$.

Figure 6 shows the ratio of the thickness of the shell of unscreened ions and the droplet radius R_0 as a function of the degree of frustration in semilogarithmic scale. The relationship according to Eq. 11 projects all data points onto a smooth curve, with their distribution along the curve given by the measured α values. The insets provide visualizations of three specific cases corresponding to (i) the limit of no frustration/pure Coulomb explosion, (ii) the onset of full frustration, and (iii) the highest degree of frustration detected in the experiment. In the insets, screened and unscreened ions are depicted as light and dark blue spheres, respectively, and neutral helium atoms are depicted as yellow.

For the smallest values of α, no electron trapping occurs, and unscreened ions are distributed homogeneously throughout the cluster ($\delta_{\mathrm{shell}} = R_0$). However, once frustration sets in, the normalized shell thickness, $\delta_{\mathrm{shell}}/R_0$, decreases rapidly from 1 to 0.15 over the range $0.67 < \alpha \lesssim 2.5$, corresponding to the transition from no to full frustration. The normalized shell thickness continues to decrease with increasing frustration, reaching a mere 0.8% of the droplet radius at $\alpha = 44$. We note that for $\alpha > 20$, the absolute shell thickness saturates at ~ 3 nm (see Appendix C). This region corresponds to the plateau observed in the $\alpha-$dependence of the $E_{\mathrm{kin}}^{\mathrm{max}}$ in Fig. 3a. Taking into account that the Coulomb potential at the cluster surface already saturates for much smaller values of $\alpha \approx 2.5$, the "delayed" saturation of $E_{\mathrm{kin}}^{\mathrm{max}}$ in Fig. 3a and the correspondence of the plateau regions for the $E_{\mathrm{kin}}^{\mathrm{max}}$ and the absolute thickness of the unscreened ion shell lends further support to the concept that both Coulomb repulsion and ion-atom collisions play important roles for determining the maximum ion E_{kin}.

The clusters studied here in a single experiment, under nominally identical experimental conditions, cover the entire range of charging conditions, from a homogeneous distribution of ions subject to mutual Coulomb repulsion to quasineutral nanoplasmas extending across $> 99\%$ of the droplet diameter. Differentiating these charged cluster varieties has only become possible through the single-pulse measurement capabilities developed at X-FELs. At the same time, they illustrate the importance of complete characterizations of light–matter interactions on a pulse-by-pulse basis in order to understand the underlying physics.

6 Conclusions

Charging and disintegration of helium nanodroplets exposed to intense soft X-ray pulses is studied by single pulse coincident ion TOF spectroscopy and small-angle X-ray scattering. Experimental conditions span from pure Coulomb explosion to a regime of deeply frustrated ionization. The low ion density due to the small X-ray absorption cross section of He leads to a complex relationship between measured ion kinetic energies and cluster ionization conditions that can only be disentangled through the coincident single-pulse measurement capability. Maximum ion kinetic energies are modeled by a combination of Coulomb repulsion from unscreened cluster ions and ion–atom collisions during the expansion. We find that the measured kinetic energies reflect on ions created deeper inside the droplet in the Coulomb explosion limit and on ions originating from the surface in the deeply frustrated, hydrodynamic limit. The results demonstrate the need for quantitative single pulse information to derive physical insight from interpreting ion TOF spectra in intense X-ray–cluster interactions.

Acknowledgements This work was supported by the Atomic, Molecular, and Optical Sciences Program of the US Department of Energy, Office of Science, Office of Basic Energy Sciences, Chemical Sciences, Geosciences and Biosciences Division, through Contract No. DE-AC02-05CH11231 (C.A.S., M.P.Z., C.Ba., A.S.C., D.M.N., O.G.) and Contract No DE-AC02-06CH11357 (MB, C.Bo.). A.J.F., C.Be., L.G., C.F.J., J.J.K., R.M.P.T, and A.F.V. were supported by the National Science Foundation under Grants no. CHE-1664990 and DMR-1701077. T.M. was supported by DFG Grant Mo 718/14-2. C.Bo. acknowledges the Swiss National Science Foundation via the National Center of Competence in Research—Molecular Ultrafast Science and Technology NCCR—MUST. Portions of this research were carried out at the LCLS, a national user facility operated by Stanford University on behalf of the U.S. DOE, OBES under beam-time Grant mo. LA12: Time-Resolved Imaging of X-ray Induced Dynamics in Clusters. Use of the Linac Coherent Light Source (LCLS), SLAC National Accelerator Laboratory, is supported by the U.S. Department of Energy, Office of Science, Office of Basic Energy Sciences under Contract No. DE-AC02-76SF00515.

Author contribution statement

CBo, AFV and OG conceived the experiment, which was performed by MPZ, CBa, MB, CBe, SC, ASC, F-JD, KRF, LG, TG, CFJ, JJK, AL, DR, RMPT, CBo, AFV and OG. CAS, AJF, MPZ, NAH, AFV and OG performed the data analysis. CAS, AJF, TG, DR, RMPT, TM, DMN, CBo, AFV and OG wrote the manuscript. All authors reviewed the final manuscript.

Appendix A: Simulation of cluster charge for partially frustrated ionization

As described in Sect. 4.1 of the main text, once the Coulomb potential (Eq. 4 of the main text) around $r = 0$ becomes sufficiently deep (i.e., the potential energy reaches about 813 eV) at some time $t = t_0$ during the X-ray-pulse, photoelectrons start to get trapped near the droplet center [17]. For $t > t_0$, continued ionization further deepens the potential and extends the range of frustrated ionization to larger radii $r_{\text{frust}}(t) > 0$. At any time $t = t_i > t_0$ during the X-ray pulse, electron trapping within the region $r \leq r_{\text{frust}}(t_i)$ leads to partial screening of the ionic background, which in turn affects the trapping potential for the remainder of the pulse, i.e, for all $t > t_i$. This mutual dependence and dynamic evolution of the droplet charge state and electron trapping potential requires a time-dependent modeling of the charging/trapping dynamics to estimate the total number of trapped electrons as a result of partial frustration. To this end, an iterative, finite time step algorithm is implemented to track the evolution of the Coulomb potential within the droplet as ionization proceeds. In this model, it is assumed that trapped electrons concentrate in the deepest part of the Coulomb potential near the droplet center and efficiently screen ions generated in this region throughout the X-ray pulse. This description leads to charge distribution corresponding to a homogeneously charged spherical shell surrounding a quasi-neutral core [17]. As such, with the onset of frustration, it becomes more accurate to model the cluster Coulomb potential as that of a charged spherical shell of finite thickness:

$$V(r) = \begin{cases} -\frac{\rho_{\text{He}^+}}{2\epsilon_0}(R_0^2 - R_{el}^2), & r \leq R_{el} \\ -\frac{\rho_{\text{He}^+}}{2\epsilon_0}(R_0^2 - \frac{2R_{el}^3}{3r} - \frac{r^2}{3}), & R_{el} < r < R_0 \\ -\frac{e}{4\pi\epsilon_0}\frac{N_{\text{eff}}}{r}, & r \geq R_0 \end{cases} \quad (12)$$

Here, e is the elementary charge, ϵ_0 is the permittivity of free space, r corresponds to the distance from the droplet's center, R_0 and R_{el} are the radii of the droplet and quasineutral core, respectively, ρ_{He^+} is the charge density of ions in the charged spherical shell, and N_{eff} is the net cluster charge. Since we assume a homogeneous distribution of ionization events, the ion charge density is taken to be $\rho_{\text{He}^+} = e \cdot N_{\text{ion}}/(\frac{4}{3}\pi R_0^3)$. With continued frustrated ionization, the quasi-neutral core region expands while the thickness of the charged shell is reduced.

At the start of the simulation, the total charge is set such that the Coulomb potential is sufficiently deep to trap ionized electrons at the center of the droplet. At each step, the total charge of the droplet is increased by $+1e$, ρ_{He^+}, R_{el} and N_{eff} are updated, and the Coulomb potential is calculated as described in Eq. 12 in order to calculate the trapping threshold radius, $r_{\text{frust}}(t_i)$. The corresponding (fractional) increase in the trapped electrons at each step, ΔN_{trap}, is taken to be the product of the added charge density, ρ^+, and the volume within the trapping threshold radius:

$$\Delta N_{\text{trap}}(t_i) = \rho_+ \frac{4}{3}\pi r_{\text{frust}}^3(t_i). \quad (13)$$

The simulation progresses until the total charge equals N_{ion}, and the total number of trapped electrons is obtained by summing over the trapped electrons of all steps, leading to: $N_{\text{eff}} = N_{\text{ion}} - N_{\text{trap}} = N_{\text{ion}} - \sum_i \Delta N_{\text{trap}}(t_i)$.

The results of the simulation are also used to determine at which value of α full frustration is achieved. Note that α corresponds to the ratio of all photogenerated ions, N_{ion}, including both screened and unscreened ions, to the net charge N_{frust} of unscreened ions needed for full frustration. Thus, full frustration does not correspond to $\alpha = 1$. Instead, N_{ion} must be greater than N_{frust}, so that $N_{\text{eff}} = N_{\text{frust}}$. Using the simulation, the net charge and surface Coulomb potential is calculated for each hit, based on the size and flux extracted from the corresponding scattering image. Within the dataset herein, $\alpha \sim 2.5$ is the threshold at which the surface Coulomb potential reaches 813.4 eV, the threshold for electron trapping throughout the droplet.

Appendix B: Scaling of $E_{\text{kin}}^{\text{max}}/U_{\text{Coul}}$ with α

Presenting $E_{\text{kin}}^{\text{max}}/U_{\text{Coul}}$ plotted against α with log–log scaling elucidates a linear trend, with a slope 0.47, as shown in Fig. 7. This indicates that $E_{\text{kin}}^{\text{max}}/U_{\text{Coul}} \propto \sqrt{\alpha}$. As such, we use this scaling to plot a trend line in Fig. 4 of the main text. Analysis of this relationship is beyond the scope of this work.

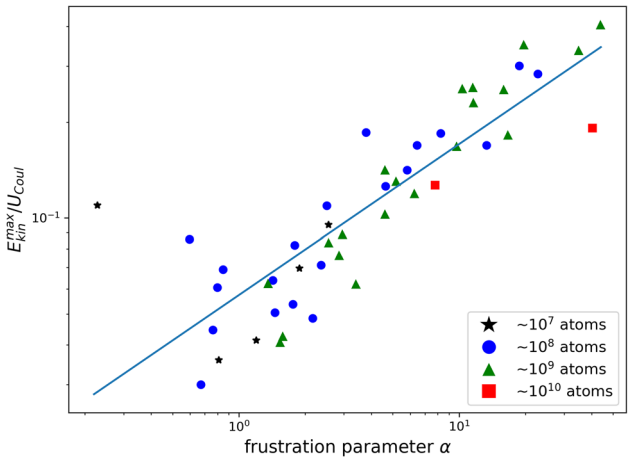

Fig. 7 Results from Fig. 4 in a log–log representation. The slope of a linear fit indicated by the blue line is 0.47, indicating that $E_{\mathrm{kin}}^{\mathrm{max}}/U_{\mathrm{Coul}} \propto \sqrt{\alpha}$

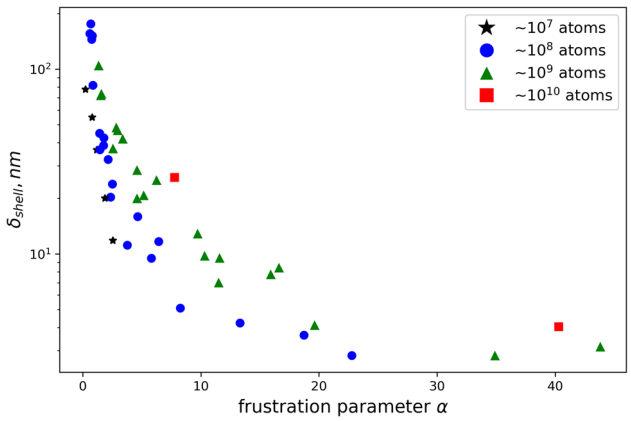

Fig. 8 Thickness of the shell of unscreened ions as a function of the frustration parameter

Appendix C: Shell Thickness of Unscreened Ions

Unscreened cations are expected to be homogeneously distributed below the onset of frustration ($\alpha < 0.67$) and begin to localize towards the surface of the charged droplet with increasing frustration. As derived from Eq. 11 in the main text, the shell thickness δ_{shell} can be expressed as

$$\delta_{\mathrm{shell}} = R_0[1 - (1 - \frac{N_{\mathrm{eff}}}{N_{\mathrm{ion}}})^{1/3}], \qquad (14)$$

where R_0 is the droplet radius, N_{ion} is the number of ions from photoionization, and N_{eff} is the net cluster charge as defined in Sect. 5.1 of the main text. In Fig. 8, the shell thickness occupied by unscreened ions is plotted as a function of the frustration parameter α.

References

1. C. Bostedt, E. Eremina, D. Rupp, M. Adolph, H. Thomas, M. Hoener, A.R.B. De Castro, J. Tiggesbäumker, K.-H. Meiwes-Broer, T. Laarmann, H. Wabnitz, E. Plönjes, R. Treusch, J.R. Schneider, T. Möller, Phys. Rev. Lett. **108**, 093401 (2012)
2. M.M. Seibert, T. Ekeberg, F.R.N.C. Maia, M. Svenda, J. Andreasson, O. Jönsson, D. Odić, B. Iwan, A. Rocker, D. Westphal, M. Hantke, D.P. Deponte, A. Barty, J. Schulz, L. Gumprecht, N. Coppola, A. Aquila, M. Liang, T.A. White, A. Martin, C. Caleman, S. Stern, C. Abergel, V. Seltzer, J. Claverie, C. Bostedt, J.D. Bozek, S. Boutet, A.A. Miahnahri, M. Messerschmidt, J. Krzywinski, G. Williams, K.O. Hodgson, M.J. Bogan, C.Y. Hampton, R.G. Sierra, D. Starodub, I. Andersson, S. Bajt, M. Barthelmess, J.C.H. Spence, P. Fromme, U. Weierstall, R. Kirian, M. Hunter, R.B. Doak, S. Marchesini, S.P. Hau-Riege, M. Frank, R.L. Shoeman, L. Lomb, S.W. Epp, R. Hartmann, D. Rolles, A. Rudenko, C. Schmidt, L. Foucar, N. Kimmel, P. Holl, B. Rudek, B. Erk, A. Hömke, C. Reich, D. Pietschner, G. Weidenspointner, L. Strüder, G. Hauser, H. Gorke, J. Ullrich, I. Schlichting, S. Herrmann, G. Schaller, F. Schopper, H. Soltau, K.U. Kühnel, R. Andritschke, C.D. Schröter, F. Krasniqi, M. Bott, S. Schorb, D. Rupp, M. Adolph, T. Gorkhover, H. Hirsemann, G. Potdevin, H. Graafsma, B. Nilsson, H.N. Chapman, J. Hajdu, Nature **470**, 78–81 (2011)
3. L.F. Gomez, K.R. Ferguson, J.P. Cryan, C. Bacellar, R.M.P. Tanyag, C. Jones, S. Schorb, D. Anielski, A. Belkacem, C. Bernando, R. Boll, J. Bozek, S. Carron, G. Chen, T. Delmas, L. Englert, S.W. Epp, B. Erk, L. Foucar, R. Hartmann, A. Hexemer, M. Huth, J. Kwok, S.R. Leone, J.H.S. Ma, F.R.N.C. Maia, E. Malmerberg, S. Marchesini, D.M. Neumark, B. Poon, J. Prell, D. Rolles, B. Rudek, A. Rudenko, M. Seifrid, K.R. Siefermann, F.P. Sturm, M. Swiggers, J. Ullrich, F. Weise, P. Zwart, C. Bostedt, O. Gessner, A.F. Vilesov, Science **345**, 906–909 (2014)
4. T. Gorkhover, M. Adolph, D. Rupp, S. Schorb, S.W. Epp, B. Erk, L. Foucar, R. Hartmann, N. Kimmel, K.U. Kühnel, D. Rolles, B. Rudek, A. Rudenko, R. Andritschke, A. Aquila, J.D. Bozek, N. Coppola, T. Erke, F. Filsinger, H. Gorke, H. Graafsma, L. Gumprecht, G. Hauser, S. Herrmann, H. Hirsemann, A. Hömke, P. Holl, C. Kaiser, F. Krasniqi, J.H. Meyer, M. Matysek, M. Messerschmidt, D. Miessner, B. Nilsson, D. Pietschner, G. Potdevin, C. Reich, G. Schaller, C. Schmidt, F. Schopper, C.D. Schröter, J. Schulz, H. Soltau, G. Weidenspointner, I. Schlichting, L. Strüder, J. Ullrich, T. Möller, C. Bostedt, Phys. Rev. Lett. **108**, 245005 (2012)
5. R. Neutze, R. Wouts, D.V.D. Spoel, E. Weckert, J. Hajdu, Nature **406**, 752–757 (2000)
6. P.J. Ho, B.J. Daurer, M.F. Hantke, J. Bielecki, A.A. Haddad, M. Bucher, G. Doumy, K.R. Ferguson, L. Flückiger, T. Gorkhover, B. Iwan, C. Knight, S. Moeller, T. Osipov, D. Ray, S.H. Southworth, M. Svenda, N. Timneanu, A. Ulmer, P. Walter, J. Hajdu, L. Young, F.R.N.C. Maia, C. Bostedt, Nat. Commun. **11**, 167 (2020)
7. D. Rupp, L. Flückiger, M. Adolph, A. Colombo, T. Gorkhover, M. Harmand, M. Krikunova, J.P. Müller, T. Oelze, Y. Ovcharenko, M. Richter, M. Sauppe, S. Schorb, R. Treusch, D. Wolter, C. Bostedt, T. Möller, Struct. Dyn. **7**, 034303 (2020)
8. C. Bostedt, H. Thomas, M. Hoener, E. Eremina, T. Fennel, K.H. Meiwes-Broer, H. Wabnitz, M. Kuhlmann, E.

Plönjes, K. Tiedtke, R. Treusch, J. Feldhaus, A.R.B. De Castro, T. Möller, Phys. Rev. Lett. **100**, 133401 (2008)
9. M. Arbeiter, T. Fennel, New J. Phys. **13**, 053022 (2011)
10. U. Saalmann, J.M. Rost, Phys. Rev. Lett. **89**, 143401 (2002)
11. I. Last, J. Jortner, Phys. Rev. A **62**, 013201 (2000)
12. T. Ditmire, T. Donnelly, A.M. Rubenchik, R.W. Falcone, M.D. Perry, Phys. Rev. A **53**, 3379–3402 (1996)
13. S. Schorb, D. Rupp, M.L. Swiggers, R.N. Coffee, M. Messerschmidt, G. Williams, J.D. Bozek, S.I. Wada, O. Kornilov, T. Möller, C. Bostedt, Phys. Rev. Lett. **108**, 233401 (2012)
14. M. Lezius, S. Dobosz, D. Normand, M. Schmidt, Phys. Rev. Lett. **80**, 261–264 (1998)
15. M. Arbeiter, T. Fennel, Phys. Rev. A **82**, 013201 (2010)
16. U. Saalmann, C. Siedschlag, J.M. Rost, J. Phys. B At. Mol. Opt. Phys. **39**, R39–R77 (2006)
17. U. Saalmann, J. Phys. B At. Mol. Opt. Phys. **43**, 194012 (2010)
18. T. Ditmire, T.W.G. Tisch, E. Springate, M.B. Mason, N. Hay, J.P. Marangos, M.H.R. Hutchinson, Phys. Rev. Lett. **78**, 2732–2735 (1997)
19. T. Fennel, K.-H. Meiwes-Broer, J. Tiggesbäumker, P.-G. Reinhard, P.M. Dinh, E. Suraud, Rev. Mod. Phys. **82**, 1793–1842 (2010)
20. T. Ditmire, J.W.G. Tisch, E. Springate, M.B. Mason, N. Hay, R.A. Smith, J. Marangos, M.H.R. Hutchinson, Nature **386**, 54–56 (1997)
21. D. Rupp, L. Flückiger, M. Adolph, T. Gorkhover, M. Krikunova, J.P. Müller, M. Müller, T. Oelze, Y. Ovcharenko, B. Röben, M. Sauppe, S. Schorb, D. Wolter, R. Mitzner, M. Wöstmann, S. Roling, M. Harmand, R. Treusch, M. Arbeiter, T. Fennel, C. Bostedt, T. Möller, Phys. Rev. Lett. **117**, 153401 (2016)
22. H. Thomas, A. Helal, K. Hoffmann, N. Kandadai, J. Keto, J. Andreasson, B. Iwan, M. Seibert, N. Timneanu, J. Hajdu, M. Adolph, T. Gorkhover, D. Rupp, S. Schorb, T. Möller, G. Doumy, L.F. Dimauro, M. Hoener, B. Murphy, N. Berrah, M. Messerschmidt, J. Bozek, C. Bostedt, T. Ditmire, Phys. Rev. Lett. **108**, 133401 (2012)
23. M. Hoener, C. Bostedt, H. Thomas, L. Landt, E. Eremina, H. Wabnitz, T. Laarmann, R. Treusch, A.R.B. De Castro, T. Möller, J. Phys. B At. Mol. Opt. Phys. **41**, 181001 (2008)
24. H. Thomas, C. Bostedt, M. Hoener, E. Eremina, H. Wabnitz, T. Laarmann, E. Plönjes, R. Treusch, A.R.B. De Castro, T. Möller, J. Phys. B At. Mol. Opt. Phys. **42**, 134018 (2009)
25. R.P. Madden, K. Codling, Phys. Rev. Lett. **10**, 516–518 (1963)
26. J.A.R. Samson, W.C. Stolte, Z.-X. He, J.N. Cutler, Y. Lu, R.J. Bartlett, Phys. Rev. A **57**, 1906–1911 (1998)
27. R.M.P. Tanyag, C. Bernando, C.F. Jones, C. Bacellar, K.R. Ferguson, D. Anielski, R. Boll, S. Carron, J.P. Cryan, L. Englert, S.W. Epp, B. Erk, L. Foucar, L.F. Gomez, R. Hartmann, D.M. Neumark, D. Rolles, B. Rudek, A. Rudenko, K.R. Siefermann, J. Ullrich, F. Weise, C. Bostedt, O. Gessner, A.F. Vilesov, Struct. Dyn. **2**, 051102 (2015)
28. T. Osipov, C. Bostedt, J.C. Castagna, K.R. Ferguson, M. Bucher, S.C. Montero, M.L. Swiggers, R. Obaid, D. Rolles, A. Rudenko, J.D. Bozek, N. Berrah, Rev. Sci. Instrum. **89**, 035112 (2018)
29. K.R. Ferguson, M. Bucher, J.D. Bozek, S. Carron, J.-C. Castagna, R. Coffee, G.I. Curiel, M. Holmes, J. Krzywinski, M. Messerschmidt, M. Minitti, A. Mitra, S. Moeller, P. Noonan, T. Osipov, S. Schorb, M. Swiggers, A. Wallace, J. Yin, C. Bostedt, J. Synchrotron Rad. **22**, 492–497 (2015)
30. M. J. Bucher, Ph.D. thesis, Technical University of Berlin, (2017)
31. L.F. Gomez, E. Loginov, R. Sliter, A.F. Vilesov, J. Chem. Phys. **135**, 154201 (2011)
32. R.J. Donnelly, C.F. Barenghi, J. Phys. Chem. Ref. Data **27**, 1217–1274 (1998)
33. P. Reinhard, E. Suraud, *Introduction to Cluster Dynamics* (Wiley, Weinheim, 2004), pp. 259–266
34. C. Bernando, R.M.P. Tanyag, C. Jones, C. Bacellar, M. Bucher, K.R. Ferguson, D. Rupp, M.P. Ziemkiewicz, L.F. Gomez, A.S. Chatterley, T. Gorkhover, M. Müller, J. Bozek, S. Carron, J. Kwok, S.L. Butler, T. Möller, C. Bostedt, O. Gessner, A.F. Vilesov, Phys. Rev. B **95**, 064510 (2017)
35. D. Verma, S.M.O. O'Connell, A.J. Feinberg, S. Erukala, R.M.P. Tanyag, C. Bernando, W. Pang, C.A. Saladrigas, B.W. Toulson, M. Borgwardt, N. Shivaram, M.F. Lin, A. Al Haddad, W. Jäger, C. Bostedt, P. Walter, O. Gessner, A.F. Vilesov, Phys. Rev. B **102**, 014504 (2020)
36. D. Attwood, A. Sakdinawat, *X-rays and Extreme Ultraviolet Radiation: Principles and Applications* (Cambridge University Press, Cambridge, 2016), pp. 64–69
37. L.B. Henke, E.M. Gullikson, J.C. Davis, At. Data Nucl. Data Tables **54**, 181–342 (1993)
38. B. Erk, K. Hoffmann, N. Kandadai, A. Helal, J. Keto, T. Ditmire, Phys. Rev. A **83**, 043201 (2011)
39. B.F. Murphy, K. Hoffmann, A. Belolipetski, J. Keto, T. Ditmire, Phys. Rev. Lett. **101**, 203401 (2008)
40. K. Ishikawa, T. Blenski, Phys. Rev. A **62**, 063204 (2000)
41. C. Bostedt, H. Thomas, M. Hoener, T. Möller, U. Saalmann, I. Georgescu, C. Gnodtke, J.-M. Rost, New J. Phys. **12**, 083004 (2010)
42. M. Grech, R. Nuter, A. Mikaberidze, P. Di Cintio, L. Gremillet, E. Lefebvre, U. Saalmann, J.M. Rost, S. Skupin, Phys. Rev. E **84**, 056404 (2011)
43. I.V. Katardjiev, Nucl. Instrum. Methods Phys. Res. B **72**, 28–32 (1992)